Supporting Information:

Exciton fine structure in perovskite nanocrystals

Peter C. Sercel,*,† John L. Lyons,‡ Darshana Wickramaratne,‡ Roman Vaxenburg,¶ Noam Bernstein,‡ and Alexander L. Efros*,‡

† *Department of Applied Physics and Materials Science, California Institute of Technology, Pasadena, California 91125, USA*

‡ *Naval Research Laboratory, Washington DC 20375, USA*

¶ *Computational Materials Science Center, George Mason University, Fairfax, Virginia 22030, USA*

E-mail: psercel@caltech.edu; efros@nrl.navy.mil

Contents

S1 Rate equation analysis of photoluminescence in perovskite nanocrystals with a dark ground state

As described in the introduction of the main text, a number of studies have been performed to date on single $CsPbBr_3$ nanocrystals (NCs), measuring low temperature photoluminescence (PL)[1–4] or magneto-PL[1,2] none of which has detected the singlet " dark" ground state which is expected for the exciton fine structure determined solely by the electron hole exchange interaction. To understand the feasibility of detection of the singlet state we performed an analysis of the expected PL signal strength of the supposed ground singlet state in relation to the upper optically allowed triplet, using a rate equation analysis for the 3-level system depicted in Figure S1.[5,6] In the figure, the levels A and F denote the upper, dipole-allowed and lower, dipole-forbidden states as usual; while G denotes the crystal ground state. Non-radiative exciton decay channels are neglected based on the experimentally measured near unity quantum yield at 5 K.[3] For unity quantum yield, the ratio of the PL signals expected from the F state and the A state, S_F/S_A, is given in steady state by,[5,6]

$$\frac{S_F}{S_A} = \frac{\Gamma_F}{\Gamma_A}\frac{\gamma_0(N_B+1)+(1-f)\Gamma_A}{f\Gamma_F+\gamma_0 N_B} \ . \tag{S1}$$

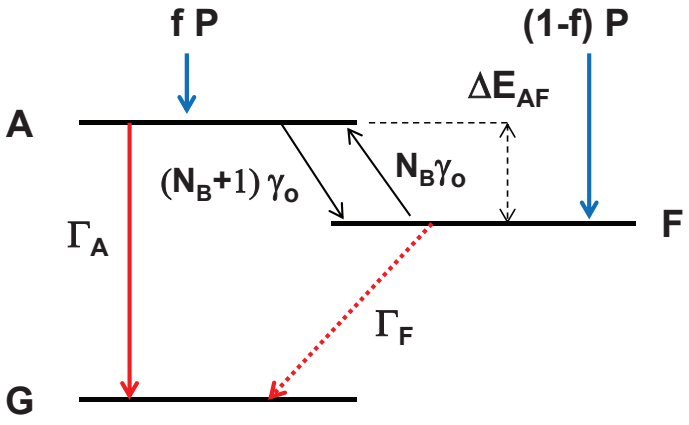

Figure S1: Cartoon showing 3-level system[5,6] for analysis of PL signal intensity of excitons in NCs with a slowly emitting ground state. Upper state A receives a fraction f of pump power P and emits at radiative rate Γ_A decaying thereby to the crystal ground state G. Slowly emitting lower state F, which has energy ΔE_{AF} below that of state A, receives fraction $(1-f)$ of pump power P and emits at a slower radiative rate Γ_F. States A and F exchange population via phonon emission/absorption at rates $\gamma_0(N_B+1)$ and $\gamma_0 N_B$ respectively, where $N_B = 1/(e^{\Delta E_{AF}}-1)$ is the Bose-Einstein phonon occupation number for phonons of energy ΔE_{AF}.[5,6]

Here, γ_0 is zero temperature rate of phonon relaxation from the A state to the F state, $N_B = 1/(e^{\Delta E_{AF}}-1)$ is the Bose-Einstein phonon occupation number for energy difference $\Delta E_{AF} = E_A - E_F$, Γ_A and Γ_F are the radiative decay rates of the states A and F, respectively, while f is the fraction of pump power feeding the upper A state. Note that this expression is the same as that obtained in a pulsed excitation arrangement by time integration of the solutions to the time-dependent rate equations. In Figure S2 we show the results of the rate equation analysis for level separations $\Delta E_{AF} = 1$ meV, panels (a, c), and for $\Delta E_{AF} = 3$ meV, panels (b,d). In Panels (a) and (b) we take the A state radiative rate, $\Gamma_A = 2.5\ \mathrm{ns}^{-1}$, corresponding to a radiative lifetime of 400 ps,[3] and the lower F state radiative rate $\Gamma_F = 10^{-2}\ \mathrm{ns}^{-1}$, corresponding to a radiative lifetime of 100 ns. The signal ratio S_F/S_A is plotted versus temperature for different scattering rates γ_0. Calculations are shown for $\gamma_0 = 1,\ 10,$ and $100\ \mathrm{ns}^{-1}$, corresponding to inter-level relaxation times ranging from 10–1000 ps. Also shown in these panels is the signal ratio expected for a thermal

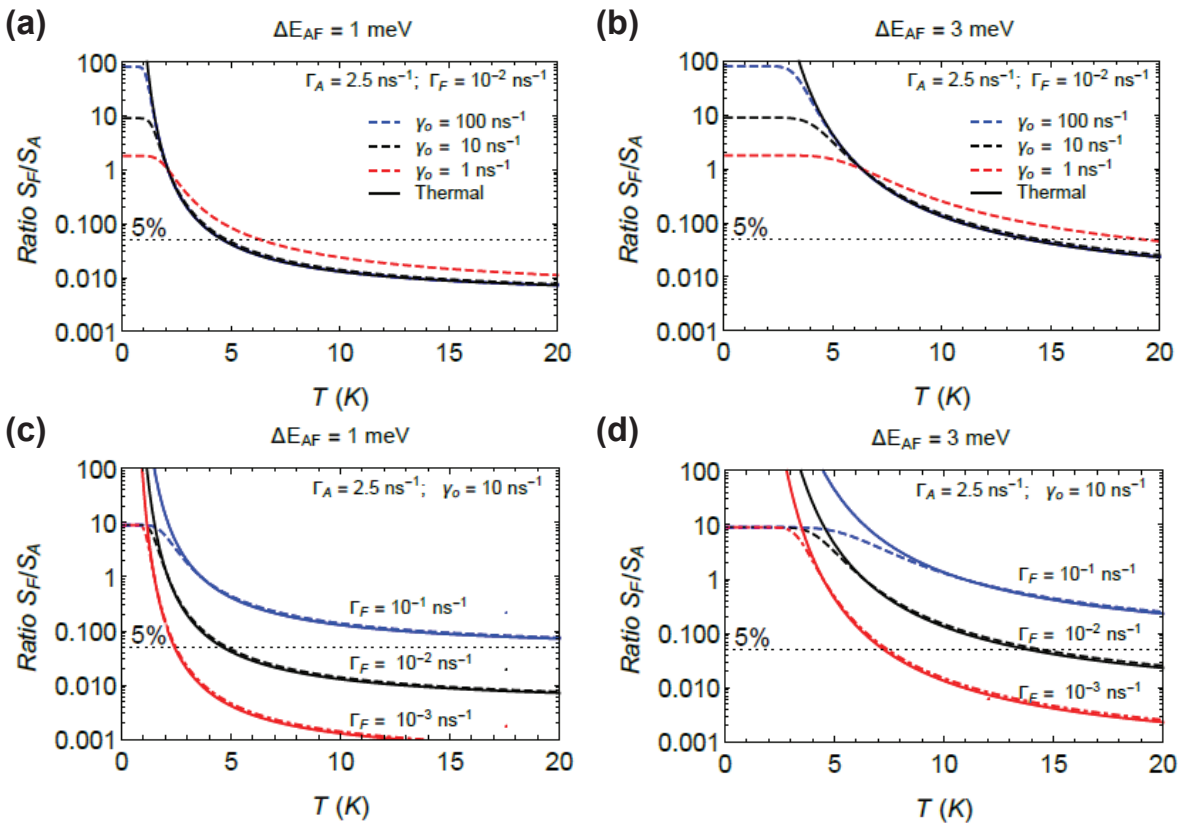

Figure S2: Ratio of temperature dependent PL signals from lower state and upper exciton states, S_F/S_A. Referring to Figure S1 for the definition of the parameters, level separation $\Delta E_{AF} = 1$ meV in panels (a) and (c), while $\Delta E_{AF} = 3$ meV in panels (b) and (d). Panels (a) and (b) show calculated results for A-state radiative rate, $\Gamma_A = 2.5\ \mathrm{ns}^{-1}$, corresponding to a radiative lifetime of 400 ps,[3] and lower F-state radiative rate $\Gamma_F = 10^{-2}\ \mathrm{ns}^{-1}$, corresponding to a radiative lifetime of 100 ns. The signal ratio S_F/S_A is plotted versus temperature for different scattering rates $\gamma_0 = 1,\ 10,$ and $100\ \mathrm{ns}^{-1}$, corresponding to inter-level relaxation times 1 ns, 100 ps, and 10 ps. Rate equation results are shown in the panels with colored dashed lines while results calculated assuming a thermal exciton population distribution are shown with solid black lines. Panels (c) and (d) show the calculated ratio S_F/S_A for $\Gamma_A = 2.5\ \mathrm{ns}^{-1}$, and relaxation rate $\gamma_0 = 10\ \mathrm{ns}^{-1}$ for lower state radiative rates $\Gamma_F = 10^{-1}$, 10^{-2}, and $10^{-3}\ \mathrm{ns}^{-1}$, corresponding to decay times of 10 ns, 100 ns, and 1 μs, respectively. Dashed lines show results calculated using the rate equation analysis while solid lines are calculated assuming a thermal exciton population distribution. The fraction f of the pump feeding the upper A state is taken as 0.5 in the calculations shown.

distribution of population between the A and F states. The fraction f of the pump power feeding the upper A state is taken as 0.5 for all panels in the figure. The calculation shows that the rate equation result matches the result assuming a thermal population distribution

for temperatures sufficiently high that $N_B\gamma_0 \gg \Gamma_F$; for the slow decay $\Gamma_F = 10^{-2}$ ns assumed, this condition is met above 5K for all but the slowest assumed scattering rate, for which the signal S_F is enhanced relative to the thermal distribution limit for any pump fraction $f < 1$. It is clear from the figure that the lower state signal should be greater than 5% at a temperature of 5 K even for the small 1 meV level spacing shown in panel (a). As the level spacing increases, the population of the lower state and the signal S_F is preferentially enhanced. For a level spacing of 3 meV, panel (b), the F state would be detectable at the 5% level for temperatures up to 14 K.

Panels (c) and (d) show the effect of lower state radiative lifetime on the calculated ratio S_F/S_A. These panels depict results calculated for fixed $\Gamma_A = 2.5$ ns^{-1}, and relaxation rate $\gamma_0 = 10$ ns^{-1} assuming different lower state radiative rates $\Gamma_F = 10^{-1}$, 10^{-2}, and 10^{-3} ns^{-1}, corresponding to decay times of 10 ns, 100 ns, and 1 μs, respectively. Dashed lines in these panels show results calculated using the rate equation analysis while solid lines are calculated assuming a thermal exciton population distribution for reference. The calculations demonstrate that the lower state signal should be detectable at the 5% level at temperatures above 5 K for all but the slowest lower state radiative decay rate of 10^{-3} ns^{-1}. Indeed, it has recently been claimed that the lower state radiative rate for $CsPbBr_3$ is in this range,[7] however, in that report, the energy separation ΔE_{AF} inferred from a similar rate equation analysis was given as 7.7 meV. Panel (d) shows that even with ΔE_{AF} as low as 3 meV the lower state signal would still be detectable with Γ_F in the 10^{-3} ns^{-1}. The calculations shown in Figure S2 make it clear as the energy spacing ΔE_{AF} increases, detection of the slowly emitting ground exciton state becomes easier since the lower state is more heavily populated in relation to the upper state. Conversely for small energy separation ΔE_{AF} detection of the lower state is more difficult. On the other hand, in the case of small ΔE_{AF}, magnetic activation of a lower "dark" exciton state is more effective. To illustrate this we calculated the magneto-exciton fine structure for a NC of cubic symmetry in the presence of

electron hole exchange and subject to the Zeeman perturbation in magnetic field $\boldsymbol{B}$:

$$H_m = g_e \mu_B \boldsymbol{J}_e \cdot \boldsymbol{B} - g_h \mu_B \boldsymbol{S}_h \cdot \boldsymbol{B} \ . \tag{S2}$$

Here, μ_B is the Bohr magneton, g_e and g_h are the electron and hole g-factors, and $\boldsymbol{J}_e$, $\boldsymbol{S}_h$ represent the electron and hole angular momenta. Calculations were performed with the exchange splitting set to 1 meV and 3 meV, with the magnetic field taken along the z direction, and setting $g_e = 2$ and $g_h = 0.4$.[1] Using the calculated fine structure and oscillator strengths of the magnetically coupled "dark" singlet and the $J = 1, M_J = 0$ "Z" state, we determined the ratio of the PL signals expected from the singlet F state and the triplet A state, S_F/S_A, as a function of the magnetic field and temperature using Eq. S1. Results are shown in Figure S3 for temperatures 4 K and 10 K, for zero field level spacing $\Delta E_{AF} = 1$ meV in panel (a) and $\Delta E_{AF} = 3$ meV in panel (b). The zero field A-state radiative rate, Γ_A was set at 2.5 ns^{-1}, corresponding to a radiative lifetime of 400 ps,[3] as in Figure S2, while the lower F-state radiative rate Γ_F is assumed to be entirely determined by magnetic field mixing with the triplet state. Inter-level scattering rate γ_0 was set at 10 ns^{-1}, corresponding to inter-level relaxation time 100 ps. Rate equation results are shown in the panels with colored dashed lines while results calculated assuming a thermal exciton population distribution are shown with solid lines. The plots show clearly that even for small inter-level spacing $\Delta E_{AF} = 1$ meV, the ratio of the lower "dark" to the upper "z" exciton PL signal should be unity at 4 K with a B field as low as 5 T.

S2 Exciton states in the effective mass approximation

In this section we describe the exciton wavefunction in a general form for confined NCs for later use in computing exciton fine structure. We start by considering the wavefunction for a direct exciton associated with conduction band m and valence band n whose band extrema are assumed to be located at the same point, $\boldsymbol{k}_0$, in k-space. Within the effective mass

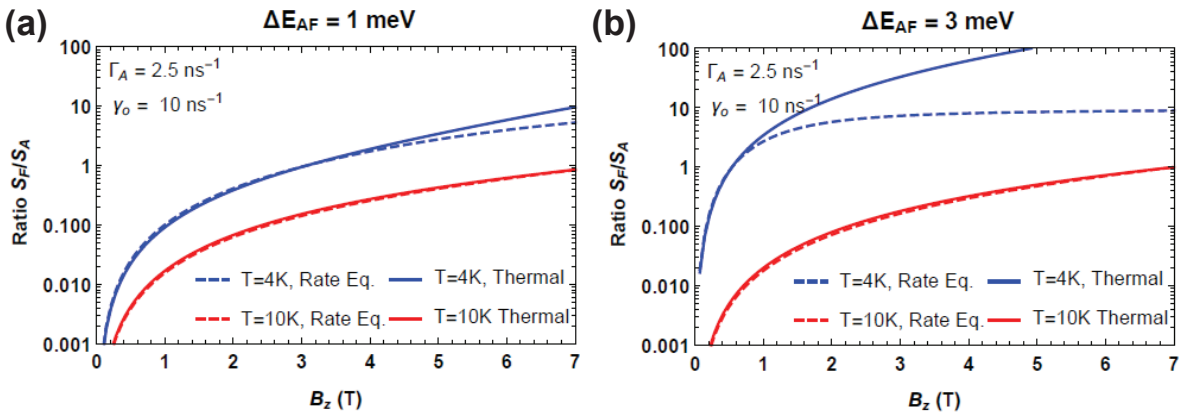

Figure S3: Magnetic field dependence of the ratio of magneto-PL signals of the lower and upper exciton states, S_F/S_A. Referring to Figure S1 for the definition of the parameters, zero-field level separation $\Delta E_{AF} = 1$ meV in panel (a) while $\Delta E_{AF} = 3$ meV in panel (b). Both panels were calculated using zero-field A-state radiative rate, $\Gamma_A = 2.5\ \mathrm{ns}^{-1}$, corresponding to a radiative lifetime of 400 ps,[3] while the lower F-state radiative rate Γ_F is determined in the calculation by magnetic field activation. The signal ratio S_F/S_A is plotted versus magnetic field for scattering rate $\gamma_0 = 10\ \mathrm{ns}^{-1}$, corresponding to inter-level relaxation time 100 ps. Rate equation results are shown in the panels with colored dashed lines while results calculated assuming a thermal exciton population distribution are shown with solid lines. The blue curves correspond to temperature 4 K while the red curves correspond to 10 K. The g-factors are taken as $g_e = 2$, $g_h = 0.4$. The fraction f of the pump feeding the upper A state is taken as 0.5 for all panels in the figure.

approximation, the wavefunction can be written in the electron hole representation as[8,9]

$$\psi_{m,n}(\boldsymbol{r}_e, \boldsymbol{r}_h) = \Phi_{m,n}(\boldsymbol{r}_e, \boldsymbol{r}_h) f_{mn}(\boldsymbol{r}_e, \boldsymbol{r}_h). \tag{S3}$$

Here, $\Phi_{m,n}(\boldsymbol{r}_e, \boldsymbol{r}_h)$ represents the $\boldsymbol{k}\cdot\boldsymbol{p}$ basis functions for the exciton at the band extrema at $\boldsymbol{k}_0$ and can be thought of as playing the role of a spin function for the exciton, while $f_{mn}(\boldsymbol{r}_e, \boldsymbol{r}_h)$ is the envelope function for the exciton and describes its orbital and center of mass motion. The functions $\Phi_{m,n}$ can be written in terms of the periodic Bloch functions u_m and u_n for the conduction and valence band edges, in the general form,[8,9]

$$\Phi_{m,n}(\boldsymbol{r}_e, \boldsymbol{r}_h) = e^{i\mathbf{k_0}(\boldsymbol{r}_e - \boldsymbol{r}_h)} u_m(\boldsymbol{r}_e) u_n(\boldsymbol{r}_h)\ . \tag{S4}$$

The envelope functions $f_{mn}(\boldsymbol{r}_e, \boldsymbol{r}_h)$ are found by solving the effective mass equation,[8,9]

$$\hat{H}^{eff}_{m',n';m,n} f_{m,n}(\boldsymbol{r}_e, \boldsymbol{r}_h) = E f_{m,n}(\boldsymbol{r}_e, \boldsymbol{r}_h) \tag{S5}$$

For a simple band system such as the perovskites, where there is no band degeneracy beyond the spin or Kramer's degeneracy, the effective mass Hamiltonian for the exciton is given by,

$$\hat{H}^{eff} = -\frac{\hbar^2}{2m_e}\nabla_e^2 - \frac{\hbar^2}{2m_h}\nabla_h^2 - U(\boldsymbol{r}_e, \boldsymbol{r}_e) \tag{S6}$$

In this expression, m_e and m_h are the effective masses at the band edge for the electron and hole, and $U(\boldsymbol{r}_e, \boldsymbol{r}_e) = e^2/(\epsilon|\boldsymbol{r}_e - \boldsymbol{r}_e|)$ represents the Coulomb interaction between the electron and the hole with account of screening associated with core electrons and electrons in remote bands, whose effect is captured by the dielectric function ϵ. For a consistent normalization it must be understood that the Bloch functions u_m are normalized over the unit cell of volume Ω as follows:[9]

$$\frac{1}{\Omega}\int_{\Omega} d^3r \; u^*_m(\boldsymbol{r}) u_n(\boldsymbol{r}) \equiv \delta_{m,n} \tag{S7}$$

Note then that the Bloch functions defined in this way are dimensionless.

For a bulk semiconductor of volume, V, large enough that quantum confinement effects are negligible, the solution to Eq. S5 is well known to correspond to a product of a hydrogenic function in the relative electron-hole coordinate, $\boldsymbol{r} = \boldsymbol{r}_e - \boldsymbol{r}_h$ and a plane wave function corresponding to the center-of-mass coordinate of the exciton, $\boldsymbol{R}$ with associated with wavevector $\boldsymbol{K}$. Here, $\boldsymbol{R} = [m_e\boldsymbol{r}_e + m_h\boldsymbol{r}_h]/M$, where m_e and m_h are the electron and hole effective masses, and $M = m_e + m_h$. For the exciton state associated with lowest energy relative motion, the envelope wavefunction can be written as,

$$f_{\boldsymbol{K};n,l,m}(\boldsymbol{r}_e, \boldsymbol{r}_h) = \frac{1}{\sqrt{V}} e^{i\boldsymbol{K}\cdot\boldsymbol{R}} \phi_{1s}(\boldsymbol{r}_e - \boldsymbol{r}_h) \; , \tag{S8}$$

where $\phi_{1s}(\boldsymbol{r})$ is the hydrogen ground state wavefunction with exciton Bohr radius a_x:

$$\phi_{1s}(\boldsymbol{r}) = \frac{1}{\sqrt{\pi a_x^3}} e^{-r/a_x} \ . \tag{S9}$$

Here, $a_x = a_0\epsilon/\mu$, where a_0 is the hydrogen Bohr radius, μ is the reduced mass of the exciton and ϵ is the relative dielectric constant, with corresponding binding energy B_x,

$$B_x = \frac{\mu}{\epsilon^2} Ry = \frac{\hbar^2}{2\mu a_x^2} = \frac{1}{2}\frac{e^2}{\epsilon a_x} \tag{S10}$$

where Ry is the Rydberg.

S2.1 Exciton states in confined systems

In this study we are interested specifically in excitons in confined systems. The exciton energy spectrum and the oscillator transition strength depend strongly on the relationship between the exciton Bohr radius and the NC size.[10,11] We consider the following limits: Considering system size L in relation to the exciton radius a_x, the weak confinement limit, where exciton center-of-mass motion exhibits quantum confinement but size quantization effects do not significantly perturb the electron/hole relative motion, corresponds to $L \gg a_x$; the strong confinement limit, in which single carrier confinement effects predominate, corresponds to $L < a_x$; and finally, the intermediate confinement limit where the exciton radius and the crystal size are comparable, $L \sim a_x$, which entails significant confinement effect on the carriers but with correlated electron-hole motion due to their Coulomb interaction. In all cases the exciton wavefunction can be written approximately according to Eq. S3 with Eq. S4 subject to the condition that the envelope wavefunction vanish at the NC surface, which determines the energy of the exciton state.

S2.1.1 Weak confinement

In the weak confinement regime, center-of-mass and relative motion of the exciton are separable for simple band systems so that the plane wave envelope associated with the bulk exciton states, Eq. S8 is replaced by a confined particle-in-a-box function. For the ground exciton in this regime, we can therefore write the envelope function as,

$$f_{\rm gr}^{Weak}(\boldsymbol{r}_e, \boldsymbol{r}_h) = \phi_{1s}(\boldsymbol{r})\psi_{\rm gr}(\boldsymbol{R}) \ , \tag{S11}$$

where $\psi_{\rm gr}(\boldsymbol{R})$ is the ground center-of-mass wavefunction for a particle in a box. In a cube shaped NC with edge length L this is given by,

$$\psi_{\rm gr}(\boldsymbol{R}) = \left(\frac{2}{L}\right)^{3/2} \cos(\pi X/L)\cos(\pi Y/L)\cos(\pi Z/L) \ , \tag{S12}$$

where X, Y and Z are the center of mass coordinates along the sides of the cube. The energy relative to the band gap of the ground state in a cube-shaped NC in the weak confinement regime is then,

$$E_x^{Weak} = E_g + \frac{\hbar^2}{2M}\left(\frac{3\pi^2}{L^2}\right) - B_x = E_g + B_x\left\{\frac{\mu}{M}\left(\frac{3\pi^2}{(L/a_x)^2}\right) - 1\right\} \ . \tag{S13}$$

In the second step of Eq.(S13) the energy has been written in terms of the ratio of the NC size and the exciton radius and parameterized in terms of the exciton binding energy, B_x.

S2.1.2 Strong confinement

In the strong-confinement regime, when the exciton Bohr radius a_x is much larger than the nanocrystal size L, then the ground-state wavefunctions of electrons or holes can be written in a simple band approximation as,

$$\psi_{\rm gr}(x, y, z) = (2/L)^{3/2}\cos(\pi x/L)\cos(\pi y/L)\cos(\pi z/L), \tag{S14}$$

where L is the cube edge length. Note that this has the same form as the envelope function for center of mass motion in the weak confinement limit, Eq. S12. In the absence of correlated motion between the electron and the hole, the envelope function of the exciton can be written as the product wavefunction,

$$f(\boldsymbol{r}_e, \boldsymbol{r}_h) = \psi_{\mathrm{gr}}(\boldsymbol{r}_e)\psi_{\mathrm{gr}}(\boldsymbol{r}_h). \tag{S15}$$

The exciton energy relative to the band gap, E_g, is found by computing the expectation value of the two-particle Hamiltonian, Eq. S6. For a cube shaped NC with edge length L the result in this limit is,

$$E_x^{Str} = E_g + \frac{\hbar^2}{2\mu}\left(\frac{3\pi^2}{L^2}\right) - 3.05\,\frac{e^2}{\epsilon L} = E_g + B_x\left(\frac{3\pi^2}{(L/a_x)^2} - 2\times(3.05)\frac{a_x}{L}\right). \tag{S16}$$

In the second step, as with the weak confinement regime, the energy in the strong confinement limit has be recast in terms of the ratio of the NC size to the exciton radius and parameterized in terms of the exciton binding energy, B_x.

S2.1.3 Intermediate confinement

Nanocrystals with $L \sim a_x$ are in the intermediate confinement regime, where confinement effects on the carrier energies are significant but the motion of the electron and hole are correlated to such a degree that a first order perturbation treatment of the Coulomb energy is inadequate. To model this, we write the envelope function of the confined excitons using a one-parameter ansatz function:[3]

$$f(\boldsymbol{r}_e, \boldsymbol{r}_h) = \frac{1}{\sqrt{N(\beta)}} e^{-\beta|\mathbf{r}_e - \mathbf{r}_h|}\psi_{\mathrm{gr}}(\boldsymbol{r}_e)\psi_{\mathrm{gr}}(\boldsymbol{r}_h)\ , \tag{S17}$$

Here, ψ_{gr} is the confined wavefunction of electrons and holes found previously for carriers in the strong confinement limit, Eq S14. This function satisfies the boundary condition that the

envelope function vanish at the NC surface, while the term involving β, the variational parameter, builds correlated electron-hole motion into the ansatz wavefunction. In the expression, $N(\beta)$ is a normalization factor, determined by the condition $\int d^3r_e d^3r_h f^2(\boldsymbol{r}_e, \boldsymbol{r}_h) = 1$, where the integration is performed over the volume of the NC.

In the variational approach we calculate the expectation value of the two-particle Hamiltonian, Eq. S6, in a cube with edge length L and minimize this with respect to the variational parameter β. Introducing the dimensionless variables $\tilde{\boldsymbol{r}}_e = \boldsymbol{r}_e/L$, $\tilde{\boldsymbol{r}}_h = \boldsymbol{r}_h/L$, and the dimensionless parameter $b = \beta L$, the expectation value $\langle f|\hat{H}|f\rangle$ reduces to the calculation of three dimensionless integrals. The first integral describes the average kinetic energy:

$$I_K(b) = \int_{-1/2}^{1/2} d^3\tilde{r}_1 \int_{-1/2}^{1/2} d^3\tilde{r}_2 \; e^{-b|\tilde{\boldsymbol{r}}_1 - \boldsymbol{r}_2|} \tilde{\psi_{\rm gr}}(\tilde{\boldsymbol{r}}_1)\tilde{\psi_{\rm gr}}(\tilde{\boldsymbol{r}}_2) \nabla^2_{\tilde{r}_1} e^{-b|\tilde{\boldsymbol{r}}_1 - \tilde{\boldsymbol{r}}_2|} \tilde{\psi_{\rm gr}}(\tilde{\boldsymbol{r}}_1)\tilde{\psi_{\rm gr}}(\tilde{\boldsymbol{r}}_2) \; , \qquad \text{(S18)}$$

where $\tilde{\psi_{\rm gr}}(\tilde{x}, \tilde{y}, \tilde{z}) = 2^{3/2} \cos(\pi\tilde{x}) \cos(\pi\tilde{y}) \cos(\pi\tilde{z})$. The second integral describes the average

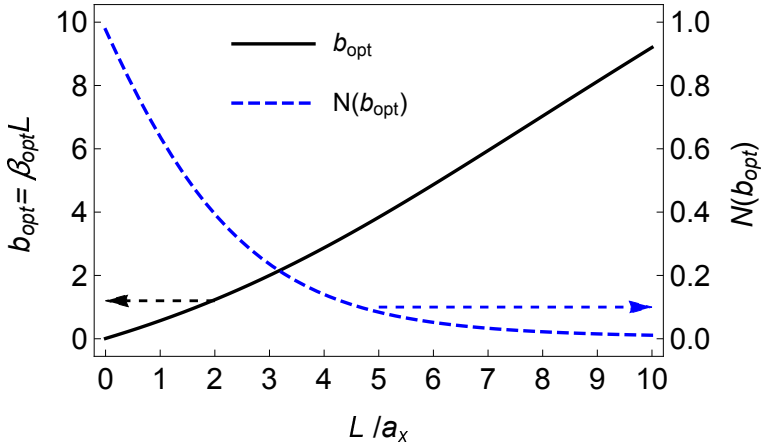

Figure S4: The size dependence of the optimum value of the variational parameter, $b_{opt} = \beta_{opt} L$, (left-hand vertical axis), and the normalization factor $N(b = b_{opt})$ (right-hand vertical axis) calculated for the exciton wave function in the intermediate confinement regime (see Eq. S17). The size dependence is plotted as function of the ratio of the edge length, L, of a cube-shaped NC to the exciton radius a_x: L/a_x.

Coulomb interaction:

$$I_C(b) = \int_{-1/2}^{1/2} d^3\tilde{r}_1 \int_{-1/2}^{1/2} d^3\tilde{r}_2 \; \frac{1}{|\tilde{\boldsymbol{r}}_1 - \tilde{\boldsymbol{r}}_2|} \left(e^{-b|\tilde{\boldsymbol{r}}_1 - \tilde{\boldsymbol{r}}_2|} \tilde{\psi_{\rm gr}}(\tilde{\boldsymbol{r}}_1)\tilde{\psi_{\rm gr}}(\tilde{\boldsymbol{r}}_2) \right)^2 \; . \qquad \text{(S19)}$$

Table S1: Exciton envelope wavefunctions, $f(\boldsymbol{r}_e, \boldsymbol{r}_h)$, and energies, E_x, for a cube-shaped perovskite NC of edge length L in different size regimes with respect to the exciton radius, a_x. The energies are parameterized in terms of the exciton binding energy, B_x, given in Eq.S10. The function $\psi_{\rm gr}(\boldsymbol{r})$ in the table is given in Eqs. S12 and S14, while $\phi_{1s}(\boldsymbol{r})$ is the ground hydrogenic function given in Eq. S9.

Regime	$f(\boldsymbol{r}_e, \boldsymbol{r}_h)$	Energy $E_x - E_g$	Eq. Ref.
Weak $L \gg a_x$	$\phi_{1s}(\boldsymbol{r}_e - \boldsymbol{r}_h)\ \psi_{\rm gr}(\boldsymbol{R})$	$B_x \left\{ \frac{\mu}{M} \left(\frac{3\pi^2}{(L/a_x)^2} \right) - 1 \right\}$	Eq. S11; Eq.S13
Inter. $L \sim a_x$	$\frac{1}{\sqrt{N(b)}} e^{-\beta\lvert\boldsymbol{r}_e - \boldsymbol{r}_h\rvert} \psi_{\rm gr}(\boldsymbol{r}_e)\psi_{\rm gr}(\boldsymbol{r}_h)$	$-\frac{1}{N(b)} \frac{B_x}{(L/a_x)^2} \left(I_K(b) + 2\frac{L}{a_x} I_C(b) \right)$	Eq. S17; Eq. S21
Strong $L < a_x$	$\psi_{\rm gr}(\boldsymbol{r}_e)\psi_{\rm gr}(\boldsymbol{r}_h)$	$B_x \left(\frac{3\pi^2}{(L/a_x)^2} - 2 \times (3.05) \frac{a_x}{L} \right)$	Eq.S15; Eq. S16

Finally, the last integral determines the dimensionless normalization constant:

$$N(b) = \int_{-1/2}^{1/2} d^3\tilde{r}_1 \int_{-1/2}^{1/2} d^3\tilde{r}_2 \ \left(e^{-b\lvert\tilde{\boldsymbol{r}}_1 - \tilde{\boldsymbol{r}}_2\rvert} \tilde{\psi_{\rm gr}}(\tilde{\boldsymbol{r}}_1)\tilde{\psi_{\rm gr}}(\tilde{\boldsymbol{r}}_2) \right)^2 \ . \tag{S20}$$

Using the integrals defined in Eqs. (S18), (S19), and (S20), we can rewrite the exciton energy relative to the band gap, E_g as,

$$E_x = E_g - \frac{\hbar^2}{2\mu L^2} \frac{I_K(b)}{N(b)} + \frac{e^2}{\epsilon L} \frac{I_C(b)}{N(b)} = -\frac{1}{N(b)} \frac{B_x}{(L/a_x)^2} \left(I_K(b) + 2\frac{L}{a_x} I_C(b) \right) \ . \tag{S21}$$

We calculated the dependence of all three $I_K(b)$, $I_C(b)$ and $N(b)$ integrals on b using Monte-Carlo integration and determined the value b_{opt} of $b = \beta L$ that minimizes the energy for a given ratio L/a_x. The value of b_{opt} and $N(b_{opt})$ vs L/a_x is plotted in Figure S4. The exciton energy is shown in Figure S5 for the strong, intermediate and weak confinement limits, expressions for which are summarized in Table S1. From the plots it is clear that for $L >\sim 7a_x$ the intermediate confinement energy converges to that calculated in the weak confinement limit, while for $L <\sim a_x$ the energy converges to the strong confinement result. It is important however to understand that the effect of the electron-hole correlated motion

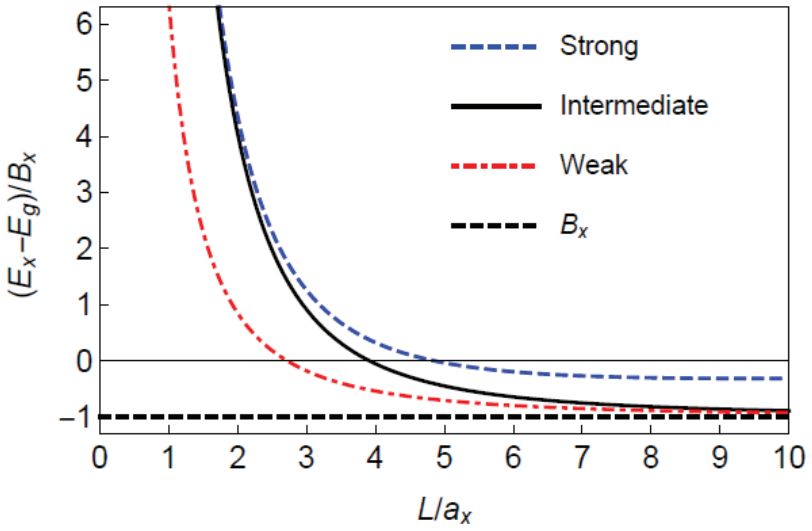

Figure S5: Exciton energy $E_x - E_g$ plotted in units of the bulk exciton binding energy, B_x, versus L/a_x, the ratio of the edge length, L of a cube-shaped NC to the exciton radius a_x. The solid black line represents the result of a variational calculation valid for the intermediate confinement limit, $L \sim a_x$. Also shown for reference are the calculated exciton energies in the strong ($L < a_x$, blue dashed line) and weak ($L \gg a_x$, red dashed line) confinement limits, and B_x (black dashed line). Expressions for the exciton energy in the various limits are summarized in Table S1.

in the intermediate confinement regime, reflected in Eq. S17, has important consequences even for sizes $L < a_x$, for example, causing significant enhancement of radiative[3] and non-radiative[12] decay rates beyond what is expected in an independent electron model such as the strong confinement approximation.

S3 Density functional theory calculations

Our first-principles calculations of $CsPbBr_3$ are based on hybrid density functional theory[13,14] (DFT) as implemented in the VASP code.[15] These calculations employed projector augmented waves[16] and plane-wave cutoffs of 500 eV, together with spin-orbit coupling (SOC). For the Pb pseudopotentials, semicore $5d$ states were included as valence electrons. K-point meshes of 8x8x8 were used for the cubic phase and an equivalent density mesh was employed for the tetragonal phase of $CsPbBr_3$.

Table S2: Calculated normalized lattice parameters (in Å) and direct band gaps (in eV) of $CsPbBr_3$, as determined from hybrid DFT calculations. Experimental lattice parameters from Ref . 17 are included in parentheses.

phase	a (Å)	b (Å)	c (Å)	direct band gap (eV)
cubic	–	–	5.95 (5.87)	1.75
tetragonal	–	5.84 (5.84)	6.04 (5.90)	2.18

The amount of exact exchange within the hybrid functional was set to 0.35, and a range separation parameter was set to 0.1 A^{-1} for both phases of $CsPbBr_3$. This approach allowed for quantitative accuracy of band structure calculations and momentum matrix elements without excessive computational expense. Perovskite structures for the cubic and tetragonal phase of $CsPbBr_3$ were adopted after the experimental measurements in Ref. 17, and all lattice parameters and atomic positions were subsequently relaxed to ensure self-consistency.

These hybrid functional calculations yielded normalized lattice parameters that are in good agreement with experiment (see Table S2).[17] The minimum direct band gaps calculated for the tetragonal phase is in good agreement with the 2.2-2.4 eV gaps that have been reported experimentally,[17,18] while the calculated band gap of the cubic phase (1.75 eV) is somewhat smaller.

S4 Band edge Bloch functions in 8-band K.P theory

The band edges in the cubic phase perovskites, point group O_h, are located at the R-point of the first Brillouin zone.[19] In the absence of spin, S and X, Y, Z, the orbital Bloch functions for the s-type and p-type band edge symmetry, respectively, form a good basis for representing the band–edge Bloch functions. In this basis the effect of the distortion of the unit cell carrying the structure from the cubic phase to the tetragonal or orthorhombic phase can be modelled as a strain deformation Hamiltonian. This is constructed using the

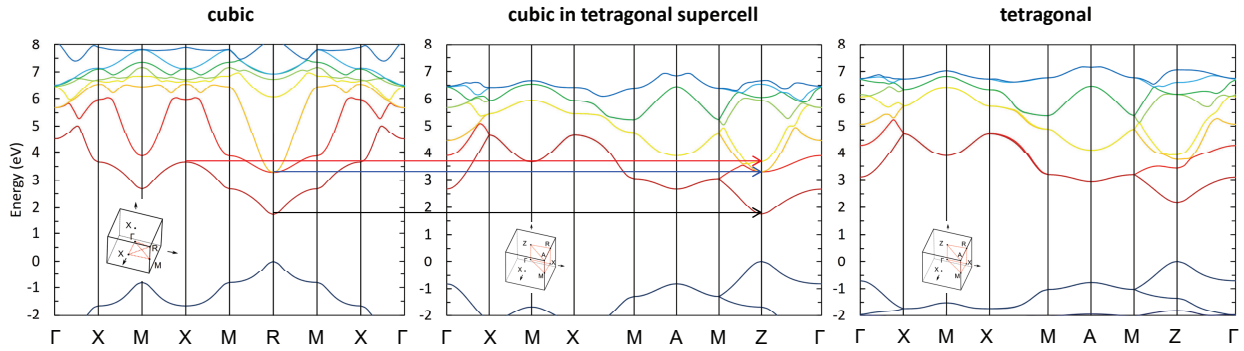

Figure S6: Energy band structure of $CsPbBr_3$ with the cubic (left and middle panels), and the tetragonal lattice structure (right panel). The middle panel shows the bandstructure of cubic phase $CsPbBr_3$ displayed in a tetragonal supercell. In cubic perovskites the edges of the conduction band (CB) and valence band (VB) are located at the R-point of the first Brillouin zone (BZ). Transition to a supercell of tetragonal symmetry results in a folding from the R-point onto the Z point of the tetragonal BZ (middle panel). The black and blue arrows show this folding of the $J = 1/2$ and $J = 3/2$ conduction bands. Additionally, the z-directed X-point of the cubic BZ becomes the Z-point of the tetragonal BZ (folding show with red arrow). As a result, CB states originating from both the R-point and the X-point of the cubic BZ reside at the Z-point of perovskites having tetragonal symmetry. This leads to a near resonance between the upper $J = 3/2$ CB states from the cubic R-point and the states derived from the X-point.

theory of invariants as,

$$\tilde{H}_d = U_d[e_{xx}L_x^2 + e_{yy}L_y^2 + e_{zz}L_z^2 - 2/3(e_{xx} + e_{yy} + e_{zz})] \tag{S22}$$

where U_d is a deformation potential and e_{ii} are the components of the strain tensor with i running over x, y, z, taken parallel to the orthorhombic cell edges. Here we are only interested in the splitting caused within the conduction band manifold and have separated out the volume dilatation term. In the basis X, Y and Z the Hamiltonian is,

$$\tilde{H}_d = \begin{pmatrix} \frac{\delta}{3} & 0 & \zeta \\ 0 & -\frac{2}{3}\delta & 0 \\ \zeta & 0 & \frac{\delta}{3} \end{pmatrix} . \tag{S23}$$

Here we have defined the tetragonal, δ, and orthorhombic, ζ crystal field parameters as:

$$\delta \equiv U_d \left(\epsilon_{zz} - \frac{\epsilon_{xx} + \epsilon_{yy}}{2} \right) \ , \ \zeta \equiv U_d \frac{\epsilon_{xx} - \epsilon_{yy}}{2} \ . \tag{S24}$$

Adding spin, the spin-orbit (SO) coupling can be written as:

$$\hat{H}_{SO} = \frac{2}{3} \Delta_{SO} \boldsymbol{L} \cdot \boldsymbol{S} \tag{S25}$$

where $\boldsymbol{L}$ is the orbital angular momentum and $\boldsymbol{S}$ is the spin. The Bloch functions which diagonalize the SO interaction can be represented as the eigenstates of total angular momentum $\boldsymbol{J} = \boldsymbol{L} + \boldsymbol{S}$. For the valence band edge, these are the even parity states of angular momentum $J = 1/2$, which we write $u^v_{1/2,\pm 1/2}$, given by:[3]

$$u^v_{1/2,1/2} = S \uparrow, \quad u^v_{1/2,-1/2} = S \downarrow, \tag{S26}$$

where the spinor functions $\uparrow$ and $\downarrow$ are the eigenfunctions of the electron spin projection operator $s_z = \pm 1/2$. The SO interaction splits the conduction band into lower, band edge, states with angular momentum $J = 1/2$, and upper states with $J = 3/2$. The conduction band edge states $u^c_{1/2,\pm 1/2}$, given by,[3]

$$u_{1/2,1/2} = \frac{-1}{\sqrt{3}} \left[(X + iY) \downarrow + Z \uparrow \right] , \qquad u_{1/2,-1/2} = \frac{1}{\sqrt{3}} \left[- (X - iY) \uparrow + Z \downarrow \right] . \tag{S27}$$

while the upper states with $J = 3/2$, $u_{3/2,\mu}$ ($\mu = \pm 3/2, \pm 1/2$) are,

$$\begin{aligned} u_{3/2,3/2} &= -\frac{1}{\sqrt{2}} (X + iY) \uparrow , & u_{3/2,-3/2} &= \frac{1}{\sqrt{2}} (X - iY) \downarrow , \\ u_{3/2,1/2} &= \frac{1}{\sqrt{6}} \left[- (X + iY) \downarrow + 2Z \uparrow \right] , & u_{3/2,-1/2} &= \frac{1}{\sqrt{6}} \left[(X - iY) \uparrow + 2Z \downarrow \right] . \end{aligned} \tag{S28}$$

In this basis, taken in the following order $|3/2,3/2\rangle$, $|3/2,1/2\rangle$, $|3/2,-1/2\rangle$, $|3/2,13/2\rangle$, $|1/2,1/2\rangle$, $|1/2,-1/2\rangle$, the conduction band Hamiltonian $\hat{H}=\hat{H}_{SO}+\hat{H}_d$ is given by[1]

$$\hat{H}(\Delta_{SO},\delta,\zeta)=\begin{pmatrix} \frac{1}{3}\Delta_{SO}+\frac{\delta}{3} & 0 & \frac{\zeta}{\sqrt{3}} & 0 & 0 & -\sqrt{\frac{2}{3}}\zeta \\ 0 & \frac{1}{3}\Delta_{SO}-\frac{\delta}{3} & 0 & \frac{\zeta}{\sqrt{3}} & \frac{\sqrt{2}\delta}{3} & 0 \\ \frac{\zeta}{\sqrt{3}} & 0 & \frac{1}{3}\Delta_{SO}-\frac{\delta}{3} & 0 & 0 & -\frac{\sqrt{2}\delta}{3} \\ 0 & \frac{\zeta}{\sqrt{3}} & 0 & \frac{1}{3}\Delta_{SO}+\frac{\delta}{3} & \sqrt{\frac{2}{3}}\zeta & 0 \\ 0 & \frac{\sqrt{2}\delta}{3} & 0 & \sqrt{\frac{2}{3}}\zeta & -\frac{2}{3}\Delta_{SO} & 0 \\ -\sqrt{\frac{2}{3}}\zeta & 0 & -\frac{\sqrt{2}\delta}{3} & 0 & 0 & -\frac{2}{3}\Delta_{SO} \end{pmatrix} \tag{S29}$$

S4.1 Tetragonal distortion

For the tetragonal phase perovskites, the crystal field parameter $\zeta=0$. The Hamiltonian can be diagonalized giving the following energies: The upper 4-fold degenerate conduction band splits into two 2-fold degenerate bands which we label, in analogy to the valence bands in III-V semiconductors, as heavy-electrons (he) with $J=3/2,\ J_z=\pm 3/2,$ and light-electrons (le) with $J=3/2,\ J_z=\pm 1/2,$ while the lower spin-orbit split off band has $J=1/2,\ J_z=\pm 1/2,$ and is labeled c for the conduction band. The energies of these bands are,,[20,22]

$$\begin{aligned} E_{le} &= -\frac{\Delta_{SO}+\delta}{6}+\frac{1}{2}\sqrt{\Delta_{SO}^2-\frac{2}{3}\Delta_{SO}\,\delta+\delta^2}; & (J_z=\pm\frac{1}{2}) \\ E_{he} &= \frac{\Delta_{SO}+\delta}{3}; & (J_z=\pm\frac{3}{2}) \\ E_c &= -\frac{\Delta_{SO}+\delta}{6}-\frac{1}{2}\sqrt{\Delta_{SO}^2-\frac{2}{3}\Delta_{SO}\,\delta+\delta^2}; & (J_z=\pm\frac{1}{2}). \end{aligned} \tag{S30}$$

The lowest conduction band, which we are chiefly interested in, has eigenstates,

$$u_{c,1/2}^{tet}=-\sin\theta Z\uparrow-\cos\theta\frac{X+iY}{\sqrt{2}}\downarrow, \qquad u_{c,-1/2}^{tet}=-\cos\theta\frac{X-iY}{\sqrt{2}}\uparrow+\sin\theta Z\downarrow \tag{S31}$$

In these expressions the angle θ is given by,[20]

$$\tan 2\theta = \frac{2\sqrt{2}\Delta_{SO}}{\Delta_{SO} - 3\delta} , \qquad (\theta \leq \frac{\pi}{2}) \; . \; . \tag{S32}$$

Following analysis of the crystal field splitting in 2-D layered perovskites[20,21] it has been suggested[4,22] that the tetragonal crystal field δ can be determined experimentally in 3-D perovskites by measurement of the splitting the upper $J = 3/2$ conduction bands. Within this model, the tetragonal crystal field, δ, splits the $J = 3/2$ conduction band states by,

$$\Delta_{tet} = E_{he} - E_{le} = \frac{\Delta + \delta}{2} - \frac{1}{2}\sqrt{\Delta_{SO}^2 - \frac{2}{3}\Delta_{SO}\,\delta + \delta^2}. \tag{S33}$$

At small δ, i.e., $\delta \ll \Delta_{SO}$, this is approximately, $\Delta_{tet} \approx \frac{2}{3}\delta$. It is easy to see that if the crystal field is positive, the "heavy electron" with $J_z = \pm 3/2$ is shifted upwards in energy with respect to the "light electron" with $J_z = \pm 1/2$.

However, this analysis assumes that the upper $J = 3/2$ conduction band splitting is determined entirely by the interactions among the 6 lowest conduction bands. As described in the main text, calculation of the band structure within DFT shows that this assumption is not valid. The upper $J = 3/2$ conduction band edges, which derive from the R-point of the Brillouin zone in the cubic phase, are close in energy to states derived from the X-point. See Figure S6 which illustrates this with the band structure calculated in DFT. As described in the main text, coupling between the $J = 3/2$ states and this X-derived conduction band enhances the upper conduction band splitting by $\sim 3\,$x beyond the result calculated within the 8-band $\boldsymbol{k} \cdot \boldsymbol{p}$ model and described by Eq. S33. The DFT calculations show, however, that the 8-band model does accurately describe the effect of the crystal field on the lowest, $J = 1/2$, conduction bands. This is a consequence of the fact that the coupling with X-band states affects the $J = 3/2$ conduction bands in the first order of perturbation theory while the J=1/2 states are affected in second order. The DFT calculated band structure splitting is well-described within a 14-band $\boldsymbol{k} \cdot \boldsymbol{p}$ model which will be described elsewhere. This

comparison is shown in Figure 4 of the main text.

Furthermore, the sign of the crystal field has been taken as *negative* in much prior work on perovskite nanocrystals,[1,4,22] that is, the "heavy electron" with $J_z = \pm 3/2$ is assumed to shift downwards in energy with respect to the "light electron" with $J_z = \pm 1/2$. This assumption has significant implications on the expected fine structure of the exciton as explored in the main text. In Ref. 22 the determination of the crystal field for 3D $MAPbI_3$ is based on the assignment of upper conduction band transitions in the absorption spectra taken from earlier work of Hirasawa et al., Ref. 23. Reviewing Ref. 23, the upper conduction band transitions were assigned for the 2D perovskite $C_{10}PbI_4$ on the basis of polarization-resolved absorption spectra, with the lower of the two bands assigned to $J_z = \pm 3/2$, corresponding to a *negative* crystal field $\delta < 0$. Indeed, we have confirmed this assignment by DFT calculations, using hybrid functionals, on a model 2D perovskite $C_{10}PbI_4$. However, measurements reported on $MAPbI_3$ in Ref. 23 showed *no polarization dependence*, so the upper band assignment in the 3D perovskite $MAPbI_3$ is indeterminate. In Ramade et al., Ref. 4, the magnitude of the crystal field in tetragonal $CsPbBr_3$ was inferred from measurements of the absorption lines involving the upper conduction bands using Eq. S33. However, the reported spectra were not polarization-resolved, presumably because these measurements were performed on randomly oriented NCs. The sign of the crystal field was taken as negative based on analogy to the 2D perovskite result of Hirasawa et al., Ref. 23 and therefore the assignment in Ref. 4 cannot be considered definitive. Our DFT calculations for tetragonal $CsPbBr_3$ indicate a positive crystal field as discussed in the main text.

S5 The electron hole exchange interaction

Three are three contributions to the electron-hole exchange interaction in cube-shaped semiconductor NCs: 1. the short-range (SR) exchange interaction, 2. the long range (LR) exchange interaction associated with the electron-hole contact interaction, and 3. the ex-

change interaction associated with the dielectric discontinuity between NCs and their surrounding medium. The total exchange constant which characterizes the magnitude of the exciton fine structure splitting can be written as the sum of these three contributions: $C^{tot} = C^{SR} + C^{LR} + C^{diel}$. Each of these contributions have been extensively discussed in the literature.[8,9,24–34]

S5.1 Short-range interaction Hamiltonian

Let us first determine the magnitude of the SR exchange constant C^{SR}. This constant was described first through phenomenologically defined Bloch functions Z of the conduction and S of the valence bands in Eqs.(S26) and (S27):

$$C^{SR} = \frac{1}{\Omega V} \int_V d^3 r_1 \int_V d^3 r_2 S(\boldsymbol{r}_1) Z(\boldsymbol{r}_2) U(\boldsymbol{r}_1, \boldsymbol{r}_2) S(\boldsymbol{r}_2) Z(\boldsymbol{r}_1) \ , \tag{S34}$$

where Ω is the volume of the unit cell, V is the NC volume, and $U(\boldsymbol{r}_1, \boldsymbol{r}_2) = e^2/[\epsilon_{SR}|\boldsymbol{r}_1 - \boldsymbol{r}_2|]$ is the Coulomb potential with short-range dielectric constant ϵ_{SR}, which, being essentially unscreened, $\epsilon_{SR} \sim 1$.[29] The integration in Eq.(S34) is taken over the entire NC volume. The unknown functional form of the Bloch function in Eq. (S34) does not allow us to use this expression for the estimation of C^{SR}. To obtain the exchange constant, we performed a direct calculation using the Bloch functions from DFT calculated as described in Sec. S3.

The SR exchange interaction can be written in a form similar to Eq. 1 in the main part of the paper. The exchange Hamiltonian is a matrix operator given by,

$$\tilde{H}^{SR}(\boldsymbol{r}_e; \boldsymbol{r}_h) = +\Omega \tilde{U}^{cell} \delta(\boldsymbol{r}_e - \boldsymbol{r}_h) \ . \tag{S35}$$

Here, the matrix $\tilde{U}^{cell}$ has matrix elements comprising exchange integrals $U^{cell}_{m',Tn;Tn',m}$ written between pairs of the Bloch functions u_m of the conduction band and Tu_n of the valence band, corresponding to the hole Bloch function u_n, where T denotes time reversal. To

calculate these matrix elements we use the analytical expression derived in Ref.:[30]

$$U^{cell}_{m',Tn;Tn',m} = \frac{1}{\Omega}\sum_{\boldsymbol{G}\neq 0}\frac{4\pi e^2}{\epsilon_{SR}G^2}\left[A_{Tn',m'}(\boldsymbol{G})\right]^{\dagger}A_{Tn,m}(\boldsymbol{G}). \tag{S36}$$

where the sum goes over all reciprocal lattice vectors $\boldsymbol{G}\neq 0$ and where

$$A_{Tn,m}(\boldsymbol{G}) \equiv \frac{1}{V}\int_V d^3r[Tu_n(\boldsymbol{r})]^* u_m(\boldsymbol{r})e^{-i\boldsymbol{G}\cdot\boldsymbol{r}}\ , \tag{S37}$$

can be calculated directly using the Bloch functions from DFT (Section 3). To determine the exchange constant C^{SR}, the resulting matrix $\tilde{U}^{cell}$ is then used in Eq. S35 and the exchange Hamiltonian for the band edge exciton is found by averaging over the exciton wavefunctions, S3. The result is,

$$\begin{aligned}\tilde{H}^{SR} &= \tilde{U}^{cell}\Omega\iint_V d^3r_e d^3r_h f^*(\boldsymbol{r}_e,\boldsymbol{r}_h)\delta(\boldsymbol{r}_e-\boldsymbol{r}_h)f(\boldsymbol{r}_e,\boldsymbol{r}_h)\\ &= \tilde{U}^{cell}\Omega\int_V d^3r|f(\boldsymbol{r},\boldsymbol{r})|^2 \equiv \tilde{U}^{cell}\Theta\ ,\end{aligned} \tag{S38}$$

where Θ is the overlap factor developed in the main text in the discussion of the SR exchange interaction. Diagonalizing this matrix we compute the energies of the ground singlet and the upper triplet excitons. We average the difference in energy between the singlet, $U_s\Theta$, and the 3 triplet exciton energies, $U_{t,i}\Theta$ where i runs over the 3 triplet states, to find,

$$\overline{\Delta E^{SR}_{st}} = \overline{\Delta U^{SR}_{st}}\Theta = \left\{\frac{\sum_{i=1}^{3}U_{t,i}}{3} - U_s\right\}\Theta\ . \tag{S39}$$

Since the average singlet-triplet splitting energy is given by the relation, $\overline{\Delta E^{SR}_{st}} = 2/3C^{SR}\Theta$, which is derived in $\boldsymbol{k}\cdot\boldsymbol{p}$ theory and has been verified using the DFT wavefunctions, the exchange constant C^{SR} is given by,

$$C^{SR} = 3/2\ \overline{\Delta U^{SR}_{st}}\ . \tag{S40}$$

S5.2 Long range exchange corrections

In addition to the $\boldsymbol{G} \neq 0$ terms in the sum used to determine the exchange constant, Eq. S36, there are terms corresponding to $\boldsymbol{G} = 0$ which create the so-called "long range" exchange interaction, which in the bulk, causes a splitting between the longitudinal and transverse optically active excitons states.[8,9,24,30] The LR exchange interaction, corresponding to the $\boldsymbol{G} = 0$ term can be represented in the coordinate $\boldsymbol{r}$ –space by the operator,[8,9]

$$\hat{H}^{LR}_{m'n';m,n}(\boldsymbol{r}'_e, \boldsymbol{r}'_h; \boldsymbol{r}_e, \boldsymbol{r}_h) = -\frac{\hbar^2}{m^2 E_g^2} U^{LR}_{m'n';m,n}(\boldsymbol{r}'_e, \boldsymbol{r}'_h; \boldsymbol{r}_e, \boldsymbol{r}_h)\delta(\boldsymbol{r}_h - \boldsymbol{r}_e)\delta(\boldsymbol{r}'_h - \boldsymbol{r}'_e) \ , \qquad \text{(S41)}$$

where the matrix element

$$U^{LR}_{m'n';m,n}(\boldsymbol{r}'_e, \boldsymbol{r}'_h; \boldsymbol{r}_e, \boldsymbol{r}_h) = \left\{ \boldsymbol{p}_{m',Tn'} \cdot \nabla_{r'_e} \left(\boldsymbol{p}_{Tn,m} \cdot \nabla_{r'_e} U(\boldsymbol{r}'_e, \boldsymbol{r}_h) \right) \right\} \ . \qquad \text{(S42)}$$

The $\hat{H}^{LR}_{m'n';m,n}$ operator in Eq. (S41) is written in the electron-hole representation and acts only on the envelope functions, $f_{mn}(r_e, r_h)$ corresponding to the total exciton wavefunction described by Eq. S3. Using the Bloch component of this wave function from Eq. S4 allows us to consider the momentum dipole transition matrix elements $\boldsymbol{p}_{m,Tn}$ as uncorrelated transitions between single-particle conduction band states with band index m and the valence band edge state Tn, which is the time reverse (T) of the hole state n. Consequently $\boldsymbol{p}_{m,Tn} = \langle \Phi_{mn} | \hat{\boldsymbol{p}} | G \rangle = \langle u_m | \hat{\boldsymbol{p}} | T u_n \rangle$, where T is the time reversal operator. The Coulomb interaction between electrons and holes in Eq.(S42): $U(\boldsymbol{r}'_e, \boldsymbol{r}_h) = e^2/(\epsilon_\infty |\boldsymbol{r}'_e - \boldsymbol{r}_h|)$ is screened by the high frequency dielectric constant ϵ_∞ since the LR interaction is occurring at length scales greater than the unit cell.[29] Averaging Eq.(S41) over the envelope wave function of the confined exciton, $f_{mn}(\boldsymbol{r}_e, \boldsymbol{r}_e)$, we estimate the magnitude of the LR exchange interaction in the NC:

$$\tilde{H}^{LR}_{m'n';m,n} = -\frac{\hbar^2}{m^2 E_g^2} \iint f^*_{m'n'}(\boldsymbol{r}'_e, \boldsymbol{r}'_e) U^{LR}_{m'n';m,n}(\boldsymbol{r}'_e, \boldsymbol{r}'_h; \boldsymbol{r}_e, \boldsymbol{r}_h) f_{mn}(\boldsymbol{r}_e, \boldsymbol{r}_e) d^3 r'_e d^3 r_e \ . \qquad \text{(S43)}$$

Relabeling $\boldsymbol{r}'_e \rightarrow \boldsymbol{r}_1$ and $\boldsymbol{r}_e \rightarrow \boldsymbol{r}_2$ we examine the integrand. Using the decomposition[25,32]

$$
\begin{aligned}
& U^{LR}_{m'n';m,n}(\boldsymbol{r}_1,\boldsymbol{r}_1;\boldsymbol{r}_2,\boldsymbol{r}_2) = \\
& \frac{e^2}{\epsilon_\infty|\boldsymbol{r}_1-\boldsymbol{r}_2|^3}\left\{\frac{3(\boldsymbol{p}_{m',Tn'}\cdot(\boldsymbol{r}_1-\boldsymbol{r}_2))(\boldsymbol{p}_{Tn,m}\cdot(\boldsymbol{r}_1-\boldsymbol{r}_2))}{|\boldsymbol{r}_1-\boldsymbol{r}_2|^2}-\mathbf{p}_{m',Tn'}\cdot\boldsymbol{p}_{Tn,m}\right\} \\
- \quad & \frac{4\pi e^2}{3\epsilon_\infty}\,\boldsymbol{p}_{m',Tn'}\cdot\boldsymbol{p}_{Tn,m}\;\delta(\boldsymbol{r}_1-\boldsymbol{r}_2)
\end{aligned}
\tag{S44}
$$

we evaluate Eq.S43 and diagonalize the resulting matrix. Note that only the third term on the right-hand side of Eq. S44, which is a *contact* term, contributes to the matrix element for cube shaped NCs as previously shown for bound excitons by Bir and Pikus.[25] In the basis of exciton states X_i, where $X_i = \{X, Y, Z, D\}$ which diagonalize the short range exchange interaction the evaluation of the LR exchange interaction results in the following expression:

$$
\tilde{H}^{LR}_{X_i} = \frac{4\pi}{3}\frac{e^2\hbar^2}{\epsilon_\infty m^2 E_g^2}|P_{cv}|^2\tilde{f}_{X_i}\frac{\Theta}{\Omega}\;. \tag{S45}
$$

Here, P_{cv} is the Kane matrix element, Θ is the overlap factor developed in the discussion of the SR exchange interaction, and the terms $\tilde{f}_{X_i}$ denote the reduced oscillator strength of exciton state X_i introduced in the main text in the discussion of the dipole matrix elements.

S5.3 Long-range exchange corrections due to dielectric discontinuity

In the discussion of the LR exchange interaction in the previous section we completely neglect the effect of the dielectric discontinuity at the NC surface. The surface dielectric discontinuity gives rise to an additional contributions to the LR exchange interaction arising from the interactions between the electron and the hole with their respective surface image charges. These corrections enhance the long range exchange interaction.[26,28,32,34]

The electron-hole Coulomb interaction in Eq. (S42) should include corrections due to

the dielectric discontinuity at the NC surface. We write these corrections as $V_{im}(\boldsymbol{r}_1, \boldsymbol{r}_2)$:

$$U(\boldsymbol{r}_1, \boldsymbol{r}_2) = \frac{e^2}{\epsilon_i |\boldsymbol{r}_2 - \boldsymbol{r}_1|} + V_{im}(\boldsymbol{r}_1, \boldsymbol{r}_2) \tag{S46}$$

Further on, we will calculate the effect of these corrections for NCs having a spherical shape. To calculate the exchange interaction we will express the two terms within Eq S46 in a multipole expansion appropriate for spherical geometry. The result for a spherical NC of radius a and dielectric constant ϵ_i surrounded by a medium of dielectric constant ϵ_o is,

$$U(\boldsymbol{r_1}, \boldsymbol{r_2}) = \frac{e^2}{\epsilon_i a} \sum_{l,m} C_l^m(r_1, r_2) Y_l^{m*}(\theta_1, \phi_1) Y_l^m(\theta_2, \phi_2), \tag{S47}$$

where $C_l^m(r_1, r_2)$ is a function of the radial coordinates only, and is given by,

$$C_l^m(r_1, r_2) \equiv \frac{4\pi}{(2l+1)} \left[\frac{a r_<^l}{r_>^{l+1}} + \frac{(\epsilon_i - \epsilon_o)(l+1)}{\epsilon_i l + \epsilon_o (l+1)} \left(\frac{r_1 r_2}{a^2} \right)^l \right]. \tag{S48}$$

Here, $r_>$ or $r_<$ is the greater or lesser of $|r_2|$ or $|r_1|$. The first term above originates from the usual direct Coulomb multipole expansion[35] while the second term represents the corrections associated with the dielectric discontinuity at the NC surface.[36]

The exchange interaction described by Eq. (S41) can be rewritten in terms of the Coulomb interaction of the optically induced charged density associated with the exciton state:[31]

$$H^{LR}_{m'n';m,n} = \frac{1}{e^2} \int_{V_1} dV_1 \int_{V_2} dV_2 \left[-\boldsymbol{\nabla}_1 \cdot \boldsymbol{P}_{m'n'}(\boldsymbol{r}_1) \right]^* U(\boldsymbol{r}_1, \boldsymbol{r}_2) \left[-\boldsymbol{\nabla}_2 \cdot \boldsymbol{P}_{mn}(\boldsymbol{r}_2) \right] \ , \tag{S49}$$

where $\boldsymbol{P}_{mn}(\boldsymbol{r}_e)$ is the dipole density connected with a transition between one of the m, n electron-hole pair states:

$$\boldsymbol{P}_{m,n}(\boldsymbol{r}_e) = i \frac{\hbar e}{m_0 E_g} \int d^3 r_h \ f_{m,n}(\boldsymbol{r}_e, \boldsymbol{r}_h) \ \boldsymbol{p}_{Tn,m} \ \delta(\boldsymbol{r}_e - \boldsymbol{r}_h) \ . \tag{S50}$$

The dipole density can be easily estimated in the weak and the strong confinement regime using the corresponding exciton wave functions from Ref.[10] In a spherical NC the exciton envelope wavefunction, $f(\boldsymbol{r}_e, \boldsymbol{r}_h)$ in the weak confinement regime ($a_x \ll a$, where a is the NC radius) can be written as

$$f(\boldsymbol{r}_e, \boldsymbol{r}_h) = \phi_{1s}(\boldsymbol{r}_e - \boldsymbol{r}_h)\sqrt{\frac{\pi}{2a^3}} j_0(\pi R/a) \tag{S51}$$

where ϕ_{1s} is the ground hydrogenic function in the exciton, R is the center of mass radial coordinate of the exciton and $j_0(x)$ is the spherical Bessel function.

Substituting the envelope wave function from Eq.(S51) into Eq.(S50) and the Coulomb potential from Eq. (S47) to Eq.(S49) we find that the exchange Hamiltonian for semiconductors with cubic lattice structure is given by,

$$\tilde{H}^{LR} = \frac{\hbar\omega_{LT}}{3}\left(1 + \frac{12}{\pi^2}\frac{\kappa - 1}{\kappa + 2}\right)\frac{1}{4}\left(\boldsymbol{\sigma}_e \cdot \boldsymbol{\sigma}_e + 3\mathbb{I}\right) \tag{S52}$$

where $\kappa = \epsilon_i/\epsilon_o$. This results in an energy shift of the triplet state given by,

$$\Delta_{st}^{LR} = \frac{\hbar\omega_{LT}}{3} + \frac{4}{\pi^2}\left(\frac{\kappa - 1}{\kappa + 2}\right)\hbar\omega_{LT} \ , \tag{S53}$$

which is in agreement with the electrodynamic analysis of Ekimov et al., Ref.[26] Note that the first term in this expression, the bulk term, originates from the contact term in Eq. S44 above, while the second term is caused by the interaction of the electron and the hole with the image charges of the opposite carrier. A similar calculation of the triplet energy shift can be conducted in the strong confinement regime ($a_x \gg a$). The result of this calculation is in agreement with the previous one reported in Refs.[28,32]

$$\Delta_{st}^{LR} = \frac{\hbar\omega_{LT}}{3}\zeta\left(1 + \frac{3}{2\pi\zeta}\frac{\kappa - 1}{\kappa + 2}\right)\cdot\frac{\pi a_x^3}{a^3} \tag{S54}$$

where $\zeta = \pi^3 \int_0^a r^2 |j_0(\pi r/a)|^4 \approx 0.672$ is a dimensionless overlap integral of the wavefunction of the strongly confined exciton.

S5.4 Long-range exchange corrections due to NC shape anisotropy

To model the effect of shape asymmetry on the LR exchange splitting of the exciton in perovskite NCs, we used Eq. S49. This approach is equivalent to the k-space analysis of Refs. 37,38. This origin of the splitting in a system with shape asymmetry can be traced to the first term on the right hand side of Eq. S44, which reflects dipole-dipole coupling. For these calculations we evaluate the polarization density of the exciton using Eq. S50. Anisotropy enters the analysis through the exciton envelope functions, which are written as in Section S-2 with a modification to reflect shape distortion from cube-shape to a right square prism shape by setting the z-dimension of the NC distinct from the x, y dimensions: $\mathcal{L}_z \neq \mathcal{L}_x = \mathcal{L}_y = \mathcal{L}$. The envelope function is then given by,

$$\psi_{\rm gr}(\boldsymbol{R}) = \left(\frac{8}{\mathcal{L}^2\mathcal{L}_z}\right)^{1/2} \cos(\pi X/\mathcal{L}) \cos(\pi Y/\mathcal{L}) \cos(\pi Z/\mathcal{L}_z) \ , \tag{S55}$$

Taking $r = \mathcal{L}_z/\mathcal{L}$, as the anisotropy parameter, we preserve NC volume $V = L^3$ by writing, $\mathcal{L}_z = Lr^{2/3}$ and $\mathcal{L}_x = \mathcal{L}_y = Lr^{-1/3}$. The analysis shows that the LR exchange energy for exciton state X_i, where $X_i = X, Y,$ or Z, can then be written,

$$H_{X_i}(r, L) = \gamma \ (C^{LR} + C^{diel}) \tilde{f}_{X_i} \mathcal{A}_{X_i}(r, L) \Theta_c(L) \tag{S56}$$

where the exchange constants C^{LR}, the dielectric discontinuity correction C^{diel}, and parameter γ are described above and in the main text; $\Theta_c(L)$ is the exchange overlap function for a cube of volume $V = L^3$, and we have defined anisotropy function $\mathcal{A}_{X_i}(L, r)$:

$$\mathcal{A}_{X_i}(r, L) \equiv \frac{3}{4\pi} \frac{\Omega I_{X_i}(r, L)}{\Theta_c(L)} \ . \tag{S57}$$

Here, the term I_{X_i} denotes exchange integrals I_Z and $I_X = I_Y$ which are given in terms of the exciton envelope functions $f(r_e, r_h)$ as,

$$I_Z = \int_{-\frac{\mathcal{L}}{2},-\frac{\mathcal{L}}{2},-\frac{\mathcal{L}_z}{2}}^{+\frac{\mathcal{L}_z}{2},\frac{\mathcal{L}}{2},\frac{\mathcal{L}}{2}} dx_1 dy_1 dz_1 \int_{-\frac{\mathcal{L}}{2},-\frac{\mathcal{L}}{2},-\frac{\mathcal{L}_z}{2}}^{+\frac{\mathcal{L}}{2},\frac{\mathcal{L}}{2},\frac{\mathcal{L}_z}{2}} dx_2 dy_2 dz_2 \left[\frac{df(r_1,r_1)}{dz_1}\right]^* \frac{1}{|\boldsymbol{r}_1 - \boldsymbol{r}_2|} \left[\frac{df(r_2,r_2)}{dz_1}\right] , \quad \text{(S58)}$$

$$I_X = \int_{-\frac{\mathcal{L}}{2},-\frac{\mathcal{L}}{2},-\frac{\mathcal{L}_z}{2}}^{+\frac{\mathcal{L}_z}{2},\frac{\mathcal{L}}{2},\frac{\mathcal{L}}{2}} dx_1 dy_1 dz_1 \int_{-\frac{\mathcal{L}}{2},-\frac{\mathcal{L}}{2},-\frac{\mathcal{L}_z}{2}}^{+\frac{\mathcal{L}}{2},\frac{\mathcal{L}}{2},\frac{\mathcal{L}_z}{2}} dx_2 dy_2 dz_2 \left[\frac{df(r_1,r_1)}{dx_1}\right]^* \frac{1}{|\boldsymbol{r}_1 - \boldsymbol{r}_2|} \left[\frac{df(r_2,r_2)}{dx_1}\right] . \quad \text{(S59)}$$

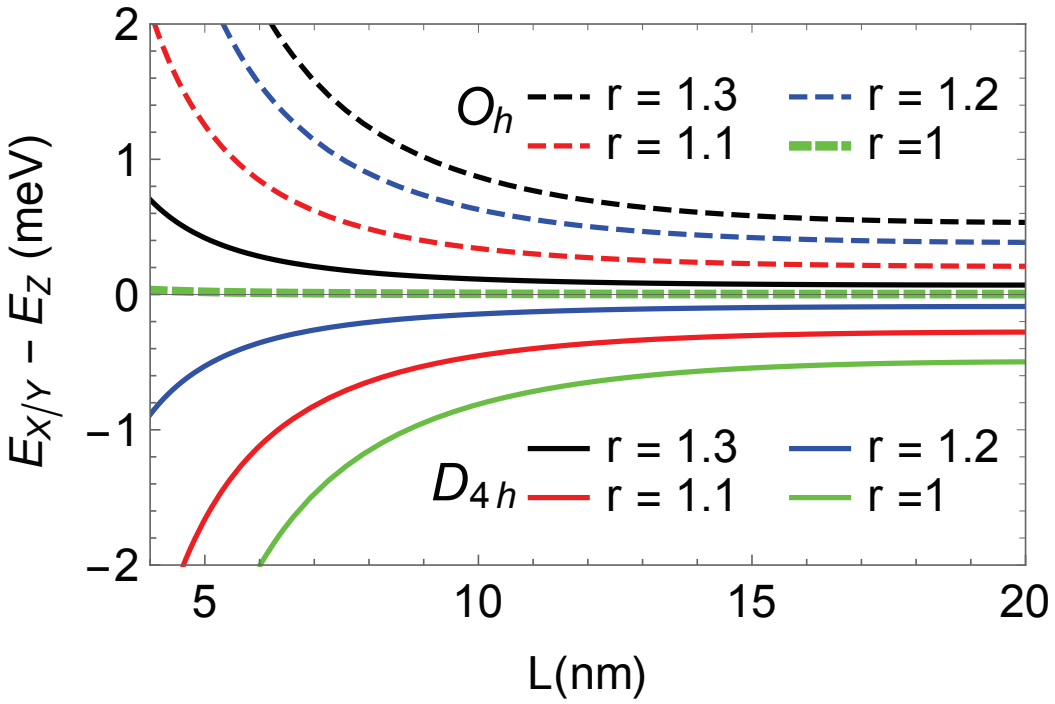

Figure S7: Size dependence of the exciton fine structure splitting $E_{X/Y} - E_Z$ created by NC shape anisotropy in $CsPbBr_3$ NCs. The calculations are conducted for NCs having right square prism shape for various uniaxial anisotropy parameters $r = L_z/L$ where $L = L_x = L_y$: $r = 1.3$, $r = 1.2$, $r = 1.1$ and $r = 1$ (no anisotropy) are shown by black, blue, and red lines respectively. The calculations conducted for NCs with crystal lattice symmetry O_h and with D_{4h} tetragonal crystal lattice symmetry, which have intrinsic crystal field splitting, are shown by dashed and solid lines respectively. The calculation is performed with LR exchange parameter $\gamma = 1$.

Evaluation of Eq. S58-S59 shows that in the strong and weak confinement regimes $\mathcal{A}(r)$ is independent of L while Θ is independent of r. We calculated the effect of anisotropy us-

ing the size dependent overlap factor $\Theta(L)$ derived for the intermediate confinement regime, plotted in Figure 2 of the main text. This amounts to neglecting dependence of the intermediate confinement normalization factor $N(\beta)$, Eq. S20, on anisotropy r, which is reasonable for small $|r-1|$ given the independence of $\mathcal{A}(r)$ in the strong ($L < a_x$) and the weak ($L \gg a_x$) confinement limits. Figure S7 shows calculated size dependence of the splitting $E_{X/Y} - E_Z$ between the X/Y doublet exciton and the Z exciton, which is expected due to shape anisotropy. Calculations were performed for fixed values of shape anisotropy r as follows: Black lines, $r = 1.3$; blue lines, $r = 1.2$; red lines, $r = 1.1$, and green lines, $r = 1$ meaning no shape anisotropy. The results are shown for NCs with O_h lattice symmetry (dashed lines) which do not have intrinsic crystal field splitting, and for NCs with D_{4h} tetragonal lattice symmetry, solid lines. Exchange parameters used are from Tables 3 and 4 of the main text, with LR exchange parameter $\gamma = 1$. Parameters reflect the effect of dielectric discontinuity which was not taken into account in Refs. 37,38 which therefore may underestimate the possible effect of the LR exchange splitting.

We find that for a uniaxial shape anisotropy $100(r-1)/r \sim 10\,\%$ the expected splitting $E_{X/Y} - E_Z$ for a 9nm NC of O_h crystal symmetry (i.e. neglecting intrinsic crystal field effects) is 0.4 meV; to obtain a splitting of 1 meV requires $100(r-1)/r \sim 30\,\%$. With parameter $\gamma = 0$, i.e., no LR exchange contribution, there is no splitting in this case. In NCs having D_{4h} crystal symmetry with the tetragonal crystal field determined by DFT the splitting is negative for all r values shown except $r = 1.3$. For reference, the reported value of the splitting in NCs of 8-10 nm size is $\sim +1$ meV[1] and in 7 nm size NCs is also $\sim +1$ meV.[4] Our calculation shows that for a 7 nm size NC having O_h symmetry the splitting is +0.6 meV with $r = 1$ and +1.1 meV with $r = 1.2$ and $\gamma = 1$, again with no splitting for $\gamma = 0$. Importantly, for an asymmetric shaped NC of fixed aspect ratio, the fine structure splitting increases with decreasing size, which can be used to distinguish this mechanism from fine structure splitting due to the Rashba effect as discussed in the main text.

References

(1) Fu, M.; Tamarat, P.; Huang,H.; Even, J.; Rogach, A.L.; and Lounis, B., *Nano Letters* **2017** *17*, 2895-2901.

(2) Isarov, M.; Tan, L. Z.; Bodnarchuk, M. I.; Kovalenko, M. V.; Rappe, A. M.; Lifshitz, E., *Nano Lett.* **2017** *17*, 5020-5026.

(3) Becker, M. A.; Vaxenburg, R.; Nedelcu, G.; Sercel, P. C.; Shabaev, A.; Mehl, M. J.; Michopoulos, J. G.; Lambrakos, S. G.; Bernstein, N.; Lyons, J. L.; Stiferle, T.; Mahrt, R. F.; Kovalenko, M. V.; Norris, D. J.; Raino, G.; Efros, Al. L. *Nature* **2018**, *553*, 189 - 193.

(4) Ramade, J.; Andriambariarijaona, L.M.; Steinmetz, V.; Goubet, N.; Legranda, L.; Barisien,T.; Bernardot,F.; Testelin, C.; Lhuillier, E.; Bramati, A.; Chamarro, M. *Nanoscale* **2018** *10*, 6393-6401.

(5) Fernee, M.J.; Littleton, B. N.; and Rubinsztein-Dunlop, H., *ACS Nano*, **2009**, *3*, 3762 -3768.

(6) Shornikova, E.V.; Biadala, L.; Yakovlev, D. R.; Sapega, V. F.; Kusrayev, Y. G.; Mitioglu, A. A.; Ballottin, M. V.; Christianen, P. C. M.; Belykh, V. V.; Kochiev, M. V.; Sibeldin, N. N.; Golovatenko, A. A.; Rodina, A. V.; Gippius, N. A.; Kuntzmann, A.; Jiang, Y.; Nasilowski, M.; Dubertreth, B.; and Bayer, M., *Nanoscale* **2018**, *10*, 646-656.

(7) Chen, L.; Li, B.; Zhang, C.; Huang, X.; Wang, X.; and Xiao, M. *Nano Letters* **2017** *18* 2074 - 2080.

(8) Pikus, G. E.; Bir, G. L. *Zh. Eksp. Teor. Fiz.* **1971**, *60*, 195-208.[*Soviet Physics JETP* **1971** *33* 108-114].

(9) Bir, G. L. and Pikus, G. E. *Symmetry and strain-induced effects in semiconductors*, Wiley (1974).

(10) Efros, Al. L.; and Efros A. L. Sov. Phys. Semicond. **1982**, *16*, 772-775.

(11) Ekimov, A. I.; Efros,Al. L.; Onushchenko, A. A. Solid State Communications **1985**, *56*, 921-924.

(12) Philbin, J. P.; and Rabani, E. *Nano Lett.* **2018** *18*, 7889-7895.

(13) Kohn, W.; and Sham, L.J., *Phys. Rev.* **1965**, *140*, A1133-A1138.

(14) Heyd, J.; Scuseria, G. E.; and Ernzerhof, M., *J. Chem. Phys.* **2003**, *118*, 8207-8215.

(15) Kresse G.; and Furthmüller, J. *Phys. Rev. B* **1996**, 54, 11169-11186.

(16) Blöchl, P. E. *Phys. Rev. B 50*, 17953-17979.

(17) Stoumpos, C. C.; Malliakas, C. D. ; Peters, J. A.; Liu, Z.; Sebastian, M. ; Im, J. ; Chasapis, T. C.; Wibowo, A. C.; Chung, D. Y.; Freeman, A. J.; Wessels, B. W.; and Kanatzidis, M. G. *Crystal Growth & Design* **2013**, *13*, 2722-2727.

(18) Pazhuk, I. P.; Pydzirailo, N. S.; and Matsko, M. G. *Sov. Phys. Sol. State* **1981**, *23*, 1263-1265.

(19) Even, J.; Pedesseau, L.; Jancu, J.-M.; and Katan, C., *J. Phys. Chem. Lett.***2013**, 4, 2999 - 3005.

(20) Nagamune, Y. ; Takeyama, S.; and Miura,N., *Phys. Rev. B* **43 1991** 12401-12405.

(21) Tanaka, K.; Takahashi, T.; Kondo,T.; Umeda, K.; Ema, K.; Umebayashi, T.; Asai, K.; Uchida, K.; and Miura, N., *Jpn. J. Appl. Phys.*, **2005**, *44*, 5923-5931.

(22) Yu,Z. G. *Sci. Rep.*, **2016**, *6*, 28576.

(23) Hirasawa, M., Ishihara, T.; Goto, T. *J. Phys. Soc. Jpn* **1994** *63*, 3870-3879.

(24) Denisov, M. M. and Makarov, V. P., *Phys. Stat. Sol. B* **1973** *56* 9-58.

(25) Pikus, G.E.; Bir, G. L. *Zh. Eksp. Teor. Fiz.* **1972**, *62*, 324-332; [*Soviet Physics JETP* **1972**, *35*, 174-178].

(26) Ekimov, A. I.; Onushchenko,A. A.; Raikh, M. E.; Efros, Al. L., *Zh. Eksp. Teor. Fiz.* **1986**, *90*, 1795-1807; [*Sov. Phys. JETP* **1986** *63* 1054-1060].

(27) Takagahara. T. *Phys. Rev. B.* **1993**, *47*, 4569 -4584.

(28) Goupalov, S. V.; Ivchenko. E. L. *J. Cryst. Growth* **1998**, *184/185*, 393 -397; *Acta Physica Polonica* **1998**, *A94*, 341-346.

(29) Franceschetti, A.; Wang, L. W.; Fu, H.; Zunger, A. *Phys. Rev. B.*, **1998** *58*, 13367-13370 (R).

(30) Rossler, U.; Trebin, H.-R. *Phys. Rev. B* **1981**, *23*, 1961-1970.

(31) Cho, K. *J. Phys. Soc. Japn.* **1999**, *68*, 683-691.

(32) Goupalov, S. V.; Ivchenko. E. L. *Fiz. Tverd. Tela* **2000**, *42*, 1976 -1984; [*Phys. Sol. Stat.* **2000** *42*, 2030-2038].

(33) Goupalov, S. V.; Ivchenko. E. L. *Fiz. Tverd. Tela* **2001**, *43*, 1791-1798 . [*Phys. Sol. Stat.* **2001**, *43*, 1867-1875].

(34) Sercel, P. C.; Efros, Al. L., *Nano Lett.***2018**, *18*, 4061-4068.

(35) Jackson, J. D. *Classical Electrodynamics*; John Wiley and Sons: New York, 1999.

(36) Kirkwood, J. G. *J. Chem. Phys.* **1934**, *2*, 351-361.

(37) Nestoklon, M. O.; Goupalov, S. V.; Dzhioev, R. I.; Ken, O. S.; Korenev, V. L.; Kusrayev, Yu. G.; Sapega, V. F.; de Weerd; Gomez, L.; Gregorkiewicz, T. ; Lin, J.; Suenaga, K.; Fujiwara, Y.; Matyushkin, L. B.; and Yassievich, I. N. *Phys. Rev. B* **2018**, *97*, 235304.

(38) Ben Aich, R.; Saidi, I.; Ben Radhia, S.; Boujdaria, K.: Barisien, T.; Legrand, L.; Bernardot, F.; Chamarro, M.; and Testelin, C. *Phys. Rev. Appl* **2019**, *11*, 034042.